applied optics

Application of the lamp mapping technique for overlap function for Raman lidar systems

Monique Walker,[1,2,*] Demetrius Venable,[3] David N. Whiteman,[2] and Tetsu Sakai[4]

[1]Goddard Earth Sciences Technology and Research, University Space Research Association, Columbia, Maryland 21044, USA
[2]Mesoscale and Atmospheric Processes, NASA Goddard Space Flight Center Greenbelt, Maryland 20771, USA
[3]Department of Physics and Astronomy Howard University, Washington, DC 20059, USA
[4]Meteorological Research Institute, Tsukuba, Ibaraki, Japan
*Corresponding author: Monique.N.Walker@Nasa.gov

Received 25 November 2015; revised 8 February 2016; accepted 16 February 2016; posted 22 February 2016 (Doc. ID 254491); published 23 March 2016

Traditionally, the lidar water vapor mixing ratio (WVMR) is corrected for overlap using data from another instrument, such as a radiosonde. Here we introduce a new experimental method to determine the overlap function using the lamp mapping technique (LMT), which relies on the lidar optics and detection system. The LMT discussed here involves a standard halogen lamp being scanned over the aperture of a Raman lidar telescope in synchronization with the lidar detection system [Appl. Opt. 50, 4622 (2011), Appl. Opt. 53, 8538 (2014)]. In this paper, we show results for a LMT-determined overlap function for individual channels, as well as a WVMR overlap function. We found that the LMT-determined WVMR overlap functions deviate within 5% of the traditional radiosonde-determined overlap. © 2016 Optical Society of America

OCIS codes: (040.5250) Photomultipliers; (120.0280) Remote sensing and sensors; (280.3640) Lidar.

http://dx.doi.org/10.1364/AO.55.002551

1. INTRODUCTION

Lidar systems are becoming frequently used in the field for atmospheric measurements because of their ability to provide superior combined temporal and spatial resolution data. Despite the lidar's ability to provide a fine-scale resolution of atmospheric data, most lidars do not receive optimum return signals from the ground to ~1 km, due to what is known as incomplete overlap. The overlap function [1,2] represents the coincidence of the backscattered signal and the receiver field of view. The overlap function is equal to one for ranges where there is complete overlap of the light and the receiver's field of view and is less than one for regions of partial or incomplete overlap. It is likely to have incomplete overlap when the transmitted laser light is close to the telescope (near field) and full overlap of the receiver when the transmitted laser light is farther away from the telescope (far field). Therefore, the overlap is a function of altitude of the light source. In general, lidar systems have incomplete overlap in the near field, which affects the accuracy of the lidar data. It is important to correct the Raman lidar–derived water vapor mixing ratio (WVMR) for incomplete overlap when studying low-level tropospheric water vapor events, such as low-level jets, planetary boundary layer, and integrated precipitable water (IPW), because most of the water vapor in the atmosphere is contained within the lower troposphere.

The traditional way for lidar scientists to correct for the WVMR overlap issue is to use radiosonde data to determine an overlap function [3]. When finding the WVMR overlap function using radiosonde data, we take the ratio of the radiosonde WVMR to the corresponding lidar WVMR profile from the ground to the region of incomplete overlap. To obtain sound statistics, this is typically done for a number of radiosonde WVMR profiles and a number of lidar WVMR profiles. Then the average of these ratios is typically used as a final overlap function (average overlap function), which is used to correct for incomplete overlap. The lidar WVMR is dependent on the radiosonde WVMR within this region when using this method.

Other methods used to determine the lidar's overlap function are optical ray-trace models [4,5], numerical models [1], and analytical models [6]. In addition, there are overlap correction techniques for the aerosol signals, which use a combination of Raman lidar backscattered signals and solutions to a lidar backscatter equation [7,8] to correct the incomplete aerosol overlap.

In this paper, we introduce a new experimental method to determine the overlap function using the lamp mapping technique (LMT), which is independent of atmospheric measurements provided by other instruments for overlap correction and relies on the lidar optics and detection system. The LMT is the scanning of a halogen lamp over the aperture of a telescope in

synchronization with the detection system. The LMT was initially developed as a means of independent calibration for Raman lidar water vapor measurements [9]. Recently, the LMT has also been used to determine glue coefficients for Raman lidar systems [10]. The motivation in this paper is to increase the accuracy of the lidar data by introducing an independent means to correct it in the lidar incomplete overlap region. The objectives in this paper are to:

(1) Demonstrate the LMT as a means of determining single-channel overlap functions for the Raman lidar water vapor, nitrogen, and aerosol channels.
(2) Demonstrate the LMT as a means of determining the overlap function for the WVMR.
(3) Compare the WVMR overlap function determined from the LMT to the WVMR overlap function determined from the radiosonde technique.

We will also compare the LMT-determined single-channel overlap to the ray-trace-determined overlap. The purpose of comparing the ray-trace model to the LMT is to further validate the method and science behind the experimental LMT determination of the overlap function.

2. METHOD

A. ALVICE

The results discussed here for the LMT-determined overlap are using NASA Atmospheric Laboratory Validation Interagency Collaboration and Education (ALVICE). The ALVICE system is composed of a Nd:YAG laser and operates at the third harmonic. ALVICE is a direct-coupled system (does not use fiber optics) and is designed to measure return signals from the lower troposphere to the lower stratosphere. ALVICE measures the Rayleigh–Mie backscattered signal of molecules and particles at ~355 nm and the Raman backscattered signals of water vapor and nitrogen molecules at ~408 and ~387 nm, respectively (Table 1). In addition, ALVICE measures aerosol depolarization, liquid/ice water scattering [11], and two pure rotational Raman signals for determining atmospheric temperature. The ALVICE system uses the narrow bandpass filters for the selection of the wanted signals and the LICEL transient recorders for data acquisition. The system parameters and laser beam characteristics for ALVICE (Table 1) are used to create an optical ray-trace model of the ALVICE system.

Table 1. ALVICE Lidar System[a]

	ALVICE
Laser emission	355 nm
Power	10–16 W
Measured light	Aerosol and Rayleigh 355 nm, water vapor 408 nm, nitrogen 387 nm, two pure rotational signals near 355 nm, parallel and perpendicular polarized 355 nm
Laser rep. rate	50 Hz
Light focus	Direct coupled
Beam waist ω_o	45 mm
Beam divergence angle α	0.1 mrad
Primary mirror diameter	600 mm
Secondary mirror diameter	158 mm
Secondary baffle	203 mm
Receiver telescope field of view	250 μrad
Aperture	0.81 mm
Focal point	821 mm
Focal length	3218 mm

[a]Coaxial telescope.

B. Optical Ray-Tracing Model of Overlap Function

In this section, we will discuss the optical ray-trace model created to determine the expected single-channel overlap function based on the ray-trace return signal and ALVICE telescope parameters. The ray-trace model was created in the Mathematica OPTICA (OPTICA 3) program using ALVICE system parameters (Table 1). The ALVICE ray-trace model is composed of an aspheric mirror for the Secondary mirror, a spherical mirror for the Primary, and an aperture stop and baffle that serves as our detector (Fig. 1). The manufacture of the laser that is used in our lidar system specifies that the laser beam profile has the characteristics of a truncated Gaussian source, which is similar to a flattop. Therefore we assumed here that the backscattered light seen by our lidar telescope has the characteristics of a flat-top source. When creating our flat-top light source in our ray-trace model, we used a variable beam waist, which grows as a function of height. We will refer to this model as "ray-trace return signal" throughout the paper. The variable beam waist described here is

$$\omega'(z) = \omega_o + (\alpha\, z), \tag{1}$$

[1,12] where ω_o is the initial laser beam waist, α is the laser beam divergence angle, and z is the height. For ALVICE, ω_o is 45 mm and α is 0.1 mrad (Table 1).

We used a function called "Point of Rays" to create the ray-trace light source with 80 rays. We also used a setting called "Fullform," which increases the number of rays by a factor squared. Therefore, when using the "Fullform" function, our input of 80 rays becomes $80^2 = 6400$ rays. The field of view (FOV) of the telescope is 250 μrad, and the corresponding aperture size for this acceptance angle (FOV) is 0.81 mm (Table 1) for the ALVICE telescope. In the ray-trace model, we set the incoming ray angles for the light source to vary larger

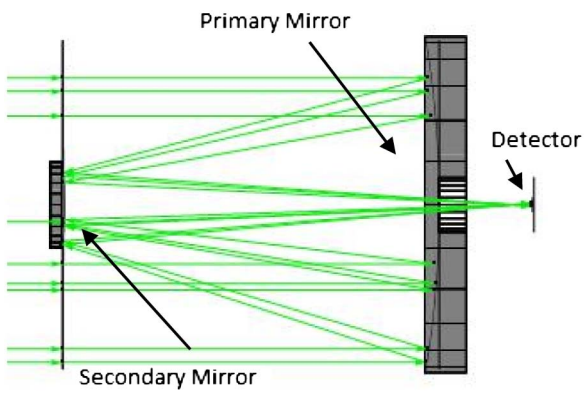

Fig. 1. Ray-trace return signal for ALVICE. See Table 1 for parameters.

than the acceptance angle of the telescope, to within 1000 μrad, to ensure that we have a reasonable distribution of rays at smaller angles (250 μrad and less).

We determined an overlap function using the ray-trace return signal of the flat-top light source and the ALVICE telescope. We define the overlap function determined from the ray-trace model as

$$O(z)_{\text{ray trace}} = \frac{S(z)_{\text{det}}}{S(z)_{\text{in}}}, \tag{2}$$

where S_{det} is the energy of the light source at the detector, and S_{in} is the energy of the light source before entering the telescope [4]. Using the ray-trace model, we determined the overlap function from 0.7 to 4.0 km using a spatial resolution of 0.1 km. Note that the ray-trace model used here to determine an overlap does not account for any loss of light due to individual channel optics; therefore, the ray-trace-determined overlap is based only on the properties of the telescope.

C. Single-Channel Overlap Function from LMT

In this section, we show how to obtain the lidar single-channel overlap function experimentally using the LMT. As we mentioned before, the LMT is when a halogen lamp is scanned over the aperture of a telescope in coincidence of the detector system (Fig. 2). To do the LMT scans, we had an X–Y translation stage with a halogen lamp mounted at 45° in the X–Y plane. We used a 45 W halogen lamp to do the LMT scans with a 10 mm scan resolution. The LMT scan used here was scanned in a square grid pattern over the telescope in which we later partitioned into various projected spot sizes to obtain the LMT overlap. When scanning over the telescope, we took a measurement in a cell-by-cell grid pattern, where each cell was considered a profile. The profile from the LMT defined here is an average count-rate value over 16,000 bins.

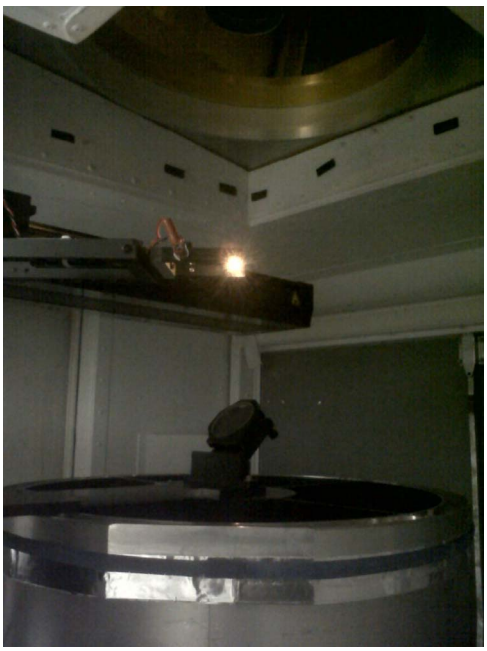

Fig. 2. Photo of halogen lamp mounted at a 45° angle over the aperture of a telescope.

The photon count rates for the LMT are defined as

$$C_j = \frac{\sum_{i=1}^{n} \text{PC}_{ij}}{Tn}, \tag{3}$$

where PC_{ij} are the photon counts corresponding to the ith bin for the jth cell of the lamp during the scan, T is the accumulation time, and n is the number of bins. So C_j are the average count rates per jth cell [10]. Then we determined the response-time corrected count rates as

$$C'_j = \frac{C_j}{(1 - \tau_r\ C_j)}. \tag{4}$$

The response-time correction value used here was $\tau_r = 5.0$ ns for ALVICE data acquisition systems [13].

After obtaining the response-time corrected photon count rates, we identified the center of our telescope within the grid count-rate data. The periscope is located over the center of the telescope and the LMT count rates over the periscope were significantly lower than the average count rates over the entire telescope.

Recall that after we conducted an LMT scan, we had a grid of counts. And in this case, we had a 600 mm by 600 mm grid. Upon identifying the center of the telescope, we began to partition the LMT grid of counts to radial spot sizes. Each spot size of the LMT data is associated with an altitude. Here we define a projected spot size as the radial area of light given as a function of height. The projected spot size can also be defined as the divergence of a light source as a function of height. An example of a projected spot size changing as a function of height would be the observation of a spot size from a flashlight on a screen. When the flashlight is close to the screen, the spot size is small. But as the flashlight is moved away from the screen, the spot size grows larger.

In this experiment, we used a 600 mm × 600 mm LMT scan with a resolution of 10 mm. Therefore we partitioned the data 10 mm radially around our central point of the telescope. Upon partitioning the data into the spot sizes, we found the overlap function. Therefore, we define the LMT overlap function for a single channel as

$$O_x(k) = \frac{\sum_{j=1}^{m} C'_{jk}}{C'_{jk_f}}, \tag{5}$$

where C'_{jk} is the average count rates within a partitioned spot size of the LMT data (the dead-time corrected count rates per j cell position for the kth partitioned spot size), x is for any channel, m is the number of cells, and C'_{jkf} is the data point used to normalize the LMT that corresponds to the minimum height at which the overlap should be equal to one.

To determine which data point is used to normalize the spot-size data from the LMT, we use the image diameter of the telescope versus the diameter of the pinhole where the light is focused. The image diameter is found using the following equation [14]:

$$d_i = \frac{(D_t + z\ \alpha)f}{z - f}, \tag{6}$$

where D_t is the diameter of the secondary or blocking baffle behind the secondary, α is the laser beam divergence, and f is the focal length of the system. This equation gives the image

spot size for each height z. When the image diameter $d_i \geq$ pinhole size, the image diameter completely fills the pinhole [14] and, therefore, the overlap should be equal to one at the corresponding heights where this condition applies. Therefore we normalize the LMT data with C'_{jk_f}, which corresponds to the minimum height where $d_i \geq$ pinhole size.

D. Ray-Trace LMT

To validate the experimental LMT method described in the previous section, we will also show results of a ray-trace model that mimics the experimental LMT. We will refer to this model as "ray-trace LMT" throughout the paper. In this model, the telescope is the same as the telescope used in the ray-trace return signal in Section 2.B (Fig. 1). However, the light source is now a single-point source with a divergence angle of 0.5 μrad and fixed at height (z axis) of ~500 mm over the telescope. We then scan the point source in the X–Y plane in a grid pattern 600 mm × 600 mm using a 10 mm step-size resolution. Using Eq. (5), we determine the overlap function for a single channel for the ray-trace LMT that mimics the experimental LMT described in the previous section. The results for the ray-trace LMT will be compared to the ray-trace return signal and experimental LMT results later in the paper.

E. Projected Spot Size to Height

Because the LMT is scanned at a fixed height over the telescope, we use the basic projected spot-size equations to determine the height associated to a given spot size. As mentioned previously, in this paper, we assume that the projected spot size seen by the telescope using the lidar signal is a flat-top spot size. Therefore, using the following equations, we find the relationship between the spot sizes of the LMT data (projected spot size on the primary mirror) $w(z)$ versus the height for a flat-top light source,

$$w(z) = \omega'(z) + \phi z, \tag{7}$$

where ω' is the beam waist defined by Eq. (1), and ϕ is the acceptance angle. Using Eq. (7) along with the ALVICE parameters (Table 1), we have determined the projected spot size and height correlation for a flat-top spot size $w(z)$ [Eq. (7)]. After determining the height to spot-size relationship, we pair the experimental LMT-partitioned data (based on the spot size) to the corresponding height.

F. LMT Overlap for the Ratio of Channels

Upon obtaining the single-channel overlap functions from the LMT, we can determine the overlap ratio for the WVMR and aerosol scattering ratio (ASR). However, in this paper, we will only discuss the overlap for the WVMR,

$$O_{\mathrm{WVMR}}(k) = \left(\frac{O_N}{O_{\mathrm{WV}}}\right), \tag{8}$$

where O_N is the single-channel overlap for the nitrogen channel, and O_{WV} is the single-channel overlap found for the water vapor channel using Eq. (5).

G. Radiosonde-Determined Overlap

Now we will discuss how we determined the WVMR overlap using radiosonde and lidar data. In this paper, we compared the WVMR overlap function determined from the radiosonde to the LMT method. Before we calculate the radiosonde-determined overlap, we first determine the best estimate (BE) lidar WVMR profile. The requirement used here for a BE lidar profile is that the random error of the WVMR is within 10%. The BE lidar profile is composed of one profile below 5 km and ~29 profiles above 10 km. Therefore this technique uses an average of profiles that vary as a function of height to generate the final BE profile. This technique is called "Var" and is explained in detail by Whiteman *et al.* [3,15].

Upon determining the BE profile, we can find the radiosonde-determined overlap function. In order to find the radiosonde-determined overlap, we take the ratio of the lidar BE WVMR to the radiosonde WVMR from the ground to the region of incomplete overlap. However, as we mentioned in the introduction, we use the average of multiple overlaps determined from the radiosonde to produce a final overlap product.

3. RESULTS

A. ALVICE Single-Channel Overlap from LMT versus Ray-Trace

First we will discuss the results of the ALVICE single-channel overlap determined using the ray-trace model versus the LMT.

As we mentioned before, the ray-trace, single-channel overlap is defined as the ratio of the signal at the detector to the incoming signal [Eq. (2)]. In Fig. 3(a), we show results comparing LMT single-channel overlaps for the nitrogen (dashed), water vapor (dotted), and perpendicular aerosol (black dots) channels and compared them to ray-trace return signal overlap function (black solid line) found using the ALVICE system parameters. The LMT single-channel overlaps were determined from the average of three LMT scans at a 10 mm step-size resolution. These scans were taken from May 23 to June 10, 2012, during a NDACC field campaign at the University of Western Ontario.

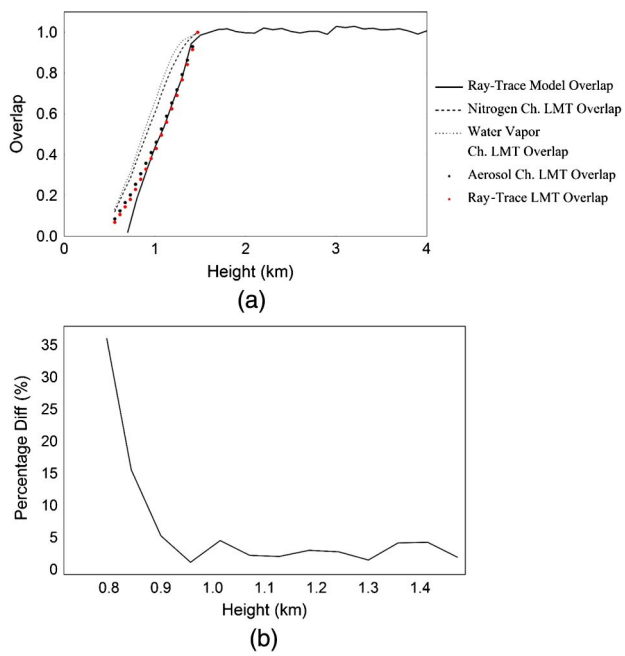

Fig. 3. (a) Plot of the single-channel overlaps determined using ray-trace models versus experimental LMT. (b) Plot is the difference of the overlaps determined from ray-trace return signal and ray-trace LMT.

We also show results from an additional ray-trace model (ray-trace LMT), which mimics the LMT in Fig. 3(a) (red dots). Both the experimental LMT overlap and the ray-trace LMT overlap data stop at ~1.5 km, because this is the height in which the telescope is fully illuminated. Therefore we expect the incomplete overlap region for ALVICE to be within ~1.5 km for single-channel determination of the overlap function. The overlap can be obtained below 0.5 km for the experimental LMT and the ray-trace LMT. However, the ray-trace return signal determined overlap begins at 0.7 km. Therefore we used the same range (starting at 0.7 km) to compare the ray-trace models and the experimental overlap for Fig. 3.

In Fig. 3(a), we also see that the experimental LMT for the aerosol perpendicular channel (black dots), ray-trace return signal overlap (black solid line), and ray-trace LMT overlap (red dots) show agreement. We also see that the experimental LMT single-channel overlap for the aerosol perpendicular channel (black dots) has a different shape than the LMT overlap for the water vapor (dotted) and nitrogen (dashed) channel. This is due to the fact that the LMT-determined overlap for the aerosol perpendicular, water vapor, and nitrogen channels responds to the different detectors and optics used in each channel, unlike the ray-trace models defined here. In this paper, the ray-trace was designed to only account for overlap influences based on the telescope design and not on the different optics and detectors in each individual channel.

Figure 3(b) shows that the ray-trace LMT and the ray-trace return signal agree within 5% from 0.9 to 1.5 km. This suggests that the traditional determination of the overlap function (overlap determined from radiosonde) and the experimental LMT-determined overlap function is expected to agree within 5% based on the ray-trace comparison in Fig. 3(b). Below 0.9 km, the agreement for the two ray-traces balloons to large values. The ray-trace return signal (black solid line) does not obtain a signal below 0.7 km, and the ray-trace LMT (red dots) receives a signal down to 0.5 km. However, we know that the ALVICE lidar can receive data as low as 0.2 km; therefore, we do not trust the ray-trace models below 0.7 km.

1. Detector Influence on Overlap Function

In the previous section, we discussed the single-channel overlaps determined using the ray-trace model and the single-channel overlap determined using the LMT. However, we want to clarify the difference found in the overlaps for the LMT and ray-trace models. As mentioned before, the ray-trace models designed here only account for the overlap function due to the telescope. But in this section, we discuss influences of the overlap due to the detector, which is captured by the LMT. In Fig. 4, we show the influences of the different detectors for the water vapor, nitrogen, and perpendicular aerosol channel. The water vapor and nitrogen channel uses the Hamamatsu photomultiplier tube (PMT) R9880U and R7400U, respectively, and the perpendicular aerosol channel uses the Hamamatsu PMT R1923. Simeonov *et al.* [16] showed that the Hamamatsu PMT 5600 series had hot spots (nonuniformity of illumination) due to the PMT design, which influences the overlap function. In detail, Simeonov *et al.* [16] showed that the grid pattern of these PMT photo sensors can contribute to these hot spots along with the orientation of the tubes, which can influence the optimization of the overlap function. The PMT 5600 series, which was used by Simeonov *et al.* [16], has a similar design to the R7400U and R9800U, which are used in ALVICE nitrogen and water vapor channels, respectively. The nonuniformity of illumination due to the photo sensors are seen as a grid pattern in Figs. 4(a) and 4(b) for the water vapor and nitrogen channels. We see that the counts per cell has a more uniform illumination for the perpendicular aerosol channel [Fig. 4(c)] than the water vapor [Fig. 4(a)] and nitrogen [Fig. 4)b)] channels. Therefore, when we partition the LMT data as shown in Figs. 4(a)–4(c), we expect a different overlap function for the water vapor, nitrogen, and aerosol channels due to the detectors, which further explains the differences seen in the LMT overlap in Fig. 3(a). We should also point out that the LMT data presented here in Figs. 4(a)–4(c) show shadowing due to the mount that is holding the lamp. The lamp is mounted on the right side of the translation stage so the residual counts appear to be shifted right due to the shadowing.

Figures 4(d) and 4(e) show the ray-trace LMT and ray-trace return signal at the primary, respectively. We see that the ray-trace LMT [Fig. 4(d)] and the ray-trace return signal at the primary [Fig. 4(e)] show a uniform illumination across the telescope as in the experimental aerosol perpendicular channel [Fig. 4(c)]. Therefore we expect the overlap shape from these three to be similar as shown Fig. 3(a).

B. LMT versus Radiosonde-Determined WVMR Overlap Function

In this section, we will discuss results of the LMT-determined WVMR overlap compared to the radiosonde-determined WVMR overlap function for ALVICE. Therefore we are comparing experimental to experimental versus experimental to ray-trace model, as in the previous section. The overlaps discussed in the previous sections were for a single channel, but in this section, we are looking at the overlap for the ratio of two channels: the nitrogen channel and the water vapor channel signal (WVMR overlap).

As mentioned before, we use Hamamatsu PMT with photo sensors in the water vapor and nitrogen channel of our lidar system. As previously stated, Simeonov *et al.* [16] has reported that these PMT have signal sensitivity due to the orientation of the PMT, which can change the overlap function. We have found this to be true in our case when using these tubes. We have a rotating shutter for both the nitrogen and water vapor channels. If care is not taken when opening these shutters, they can rotate the orientation of the tubes. We found that when the LMT scans were taken here, the PMTs were in the same orientation. The orientation of the water vapor tube was ~45° for all LMT scans as shown in Fig. 4(a).

However, during the lidar data runs, we found that some days the PMTs were accidentally rotated. Therefore we compared the average radiosonde-determined overlap function to the average LMT overlap function for the days when the PMTs were in the same orientation as when the LMTs operated. We used a total of six radiosondes to determine an average radiosonde WVMR overlap function to compare to the LMT-determined WVMR overlap function.

Figure 5 shows the overlap functions determined from the radiosonde versus the LMT. The red line is the average overlap

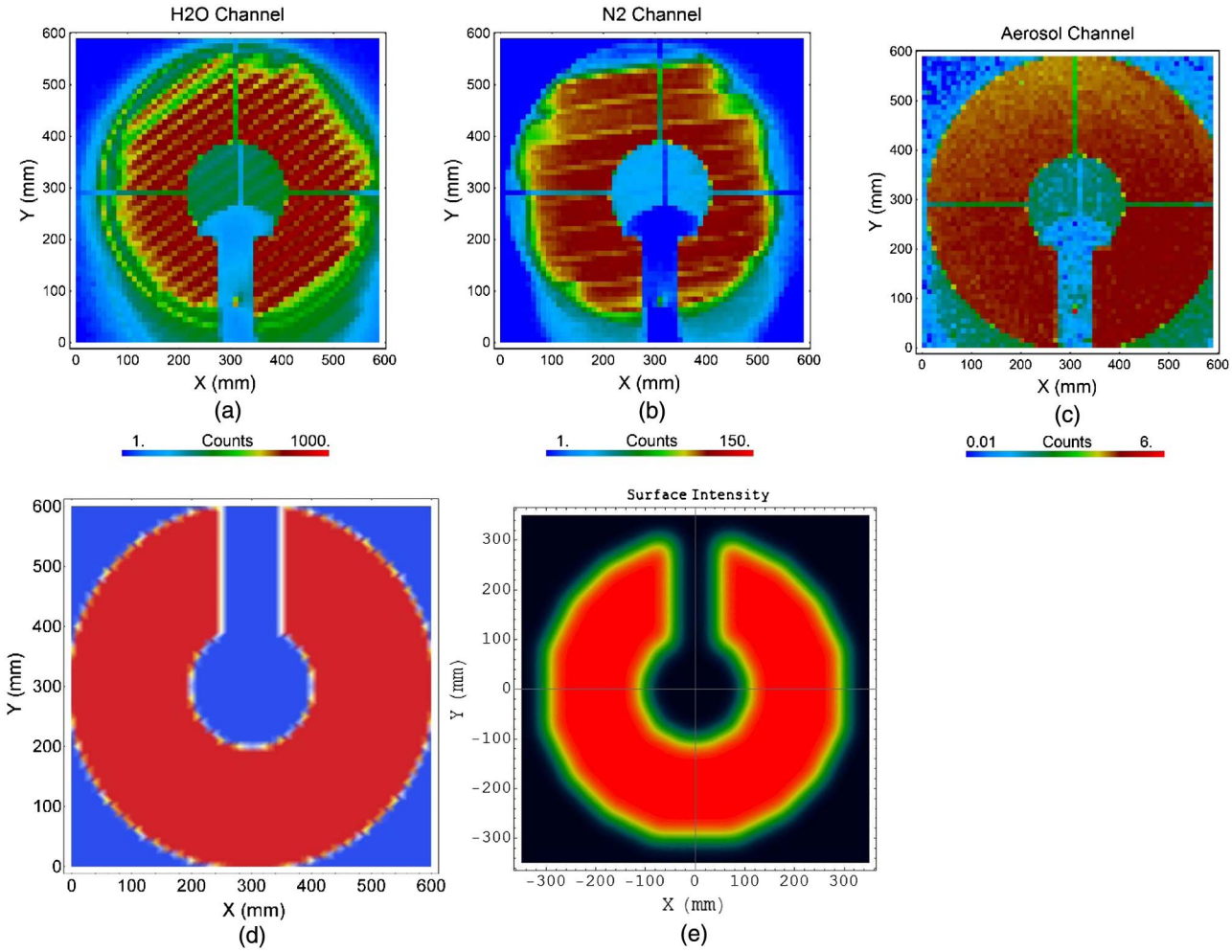

Fig. 4. (a–c) Plots are of the LMT for water vapor, nitrogen, and aerosol channels, respectively. (d–e) Plots of the ray-trace LMT and ray-trace return signal, respectively, at primary.

function determined from the three LMTs, and the black line is the average overlap function determined from the six radiosondes. The average overlap function determined from the radiosondes shows a larger variation (Fig. 5) compared to the variation of the average LMT-determined overlap. The radiosonde-determined overlap has a relative standard error (100%* standard deviation/average) of 0%–13% from 0 to 1.5 km, and the LMT-determined overlap has a relative standard error of

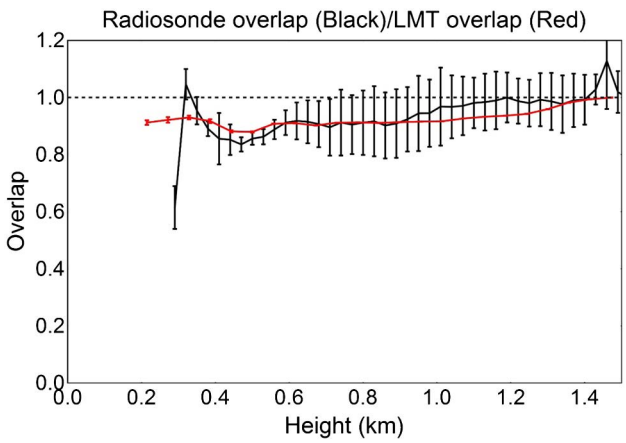

Fig. 5. Black solid line is the average overlap function of six radiosonde-determined overlap functions. The red line is the average of three LMT-determined overlap functions.

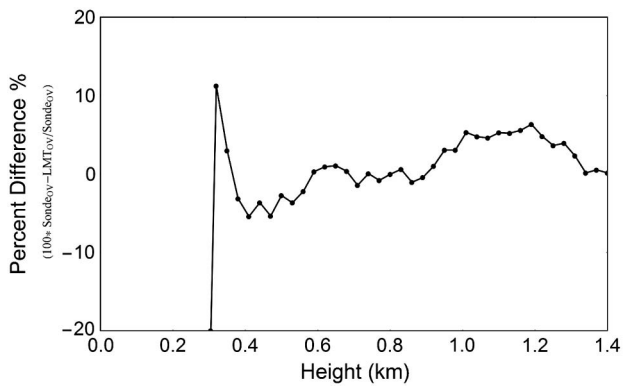

Fig. 6. Plot of relative differences between the LMT- and the radiosonde-determined overlap functions.

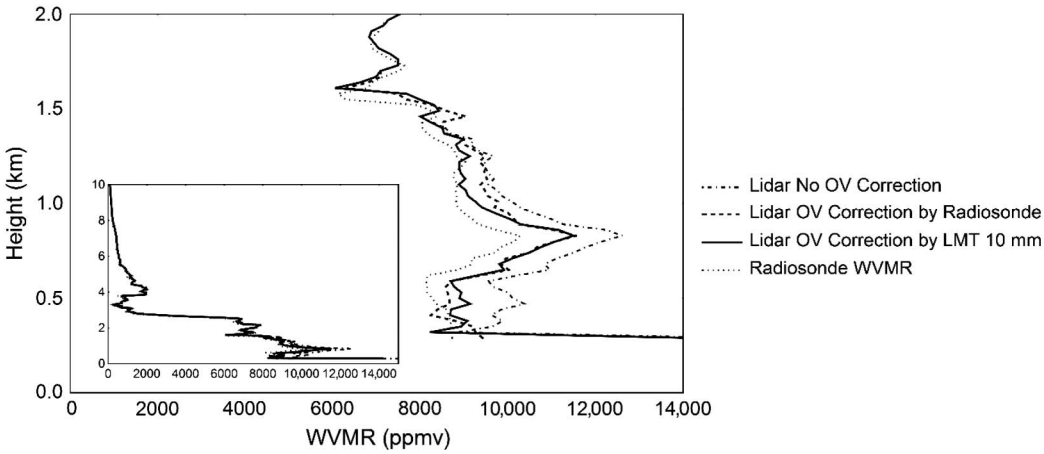

Fig. 7. ALVICE WVMR profile uncorrected for overlap is the dashed-dotted line. The solid line is the WVMR profile corrected by LMT, and the dashed line is corrected by radiosonde. The subplot shows the same profiles zoomed out.

0%–2% from 0 to 1.5 km. The variability from the radiosonde-determined overlap is due to the signal fluctuations caused by atmospheric interference of clouds and/or solar background to the lidar signal.

In Fig. 6, we have plotted the relative difference between the radiosonde-determined overlap and the LMT-determined overlap. Figure 6 shows that there is up to a 5% difference between the LMT-determined overlap function versus the average radiosonde-determined overlap function between 0.35 and 1.5 km. The sharp peak at 0.3 km is a characteristic of the laser pulse, which cannot be corrected by LMT-determined overlap because it is determined using a constant light source and not the laser.

Now we will show results of the LMT and radiosonde-determined overlap functions applied to the region of incomplete overlap for the ALVICE WVMR. Figure 7 shows an ALVICE WVMR profile that is uncorrected for overlap issues (dot-dashed line), an ALVICE WVMR profile corrected by the LMT-determined overlap (solid line), and an ALVICE WVMR profile corrected by a radiosonde-determined overlap (dashed line). The dotted line in Fig. 7 is the WVMR of the radiosonde. Figure 7 shows that the LMT-determined overlap functions and the radiosonde-determined overlap functions correct the lidar WVMR profile by shifting it to lower values of WVMR. The profile corrected using the LMT and the traditional method show a good agreement from 0.3 to 0.7 km. We begin to see the two profiles (radiosonde corrected and LMT corrected) deviate from each other by ~5% from 0.7 to 1.5 km, which is still a reasonable agreement.

4. CONCLUSION

This is the first time, to the best of our knowledge, that the single-channel overlap has been obtained experimentally using the LMT. The results above show that the ray-trace overlap and the LMT ray-trace model have similar structure and agree within 5% from 0.9 to 1.5 km. The experimental LMT was able to identify overlap function differences in each channel. However, many lidar scientists are more concerned with the ratio of the overlap functions for two channels, such as the WVMR overlap function.

To the best of our knowledge, this is the first time that the WVMR overlap has been determined using the LMT. Therefore we have introduced a new application for the LMT. The WVMR overlap determined from the LMT compared to radiosonde-determined overlap had a relative difference within 5% from 0.35 to 1.5 km. It was shown that radiosonde-determined overlap has a higher variability compared to the LMT-determined overlap. The radiosonde-determined overlap variability was due to signal fluctuations caused by atmospheric interference of clouds and or solar background to the lidar signal and had a relative standard error of up to 13% from 0 to 1.5 km.

The benefits of the LMT method are that the overlap is not influenced by atmospheric conditions and the LMT-determined overlap has low variability. This is important because the overlap function is due to alignment of the optics in the lidar system, not on atmospheric conditions. On the other hand, the LMT-determined overlap uses a fine scan resolution at 10 mm, which takes ~4 h to complete. In general practice, the LMT only takes 15 min to complete for the application of calibration, gluing, and diagnostics, but for the purpose of overlap, the scans take a long time. Therefore it is recommended that when using the LMT to determine the overlap during a campaign, that it is used once in the beginning, middle, and end of the campaign as practiced here. The LMT-determined overlap has a very small variability compared to the radiosonde-determined overlap as seen in Fig. 5; therefore, it is not necessary to do frequent fine scans for the LMT-determined overlap.

We must note that in our case, we had changes in the orientation of the PMT throughout the field campaign that caused changes in the shape of the overlap region that were tracked by the traditional method of the determination of the overlap function but not the LMT; due to the lack of frequency, we chose to run the LMT. In general, the LMT can track these changes. But due to the lack of frequency in which we operated the LMT for overlap, we did not capture the changes in the PMT orientation. Therefore we reported the overlap comparison when the PMT was in one orientation.

For systems that use the Hamamatsu PMTs that have photo sensors such as R9880U and R7400U and experience random rotation of the PMT, it is recommended to do frequent scans to capture changes or to adopt the solutions given by Simeonov *et al.*

Overall, these results show that the LMT does in fact correct the WVMR overlap and is within 5% of the radiosonde-determined overlap function. It is recommended that the traditional method be used for the determination of the WVMR overlap function for general practice. However, if lidar water vapor measurements are expected to be variable due to cloudy or daytime conditions, it is recommended that the LMT for overlap correction be used to eliminate atmospheric influences on the determination of the overlap function. Also, the LMT is recommended for the use of single-channel overlap correction for lidar system individual channels when needed.

Funding. National Aeronautics and Space Administration (NASA) Atmospheric Composition program.

Acknowledgment. Much of this research was conducted at the Howard University Beltsville Campus during the graduate studies of the senior author in the department of physics of Howard University. This research is supported by the NASA Atmospheric Composition program managed by Ken Jucks.

REFERENCES

1. T. Halldorsson and J. Langerholc, "Geometrical form factors for the lidar function," Appl. Opt. **17**, 240–244 (1978).
2. U. Wandinger, "Introduction to lidar," in *Lidar Range-Resolved Optical Remote Sensing of the Atmosphere*, C. Weitkamp, ed. (Springer, 2005), pp. 1–17.
3. D. N. Whiteman, B. Demoz, P. Girolamo, J. Comer, I. Veselovskii, K. Evans, Z. Wang, M. Cadirola, K. Rush, G. Schwemmer, B. Gentry, S. H. Melfi, B. Mielke, D. Venable, and T. Van Hove, "Raman lidar measurements during the international H_2O project. Part I: instrumentation and analysis techniques," J. Atmos. Ocean. Technol. **23**, 157–169 (2006).
4. R. Velotta, B. Bartoli, R. Capobinco, L. Fiorani, and N. Spinelli, "Analysis of the receiver response in Lidar measurements," Appl. Opt. **37**, 6999–7007 (1998).
5. D. N. Whiteman, G. Schwemmer, T. Berkoff, H. Plotkin, L. Ramos-Izquierdo, and G. Pappalardo, "Performance modeling of an airborne Raman water-vapor Lidar," Appl. Opt. **40**, 375–390 (2001).
6. H. Kuze, H. Kinjo, Y. Sakurada, and N. Takeuchi, "Field of view dependence of lidar signals by use of Newtonian and Cassegrainian telescopes," Appl. Opt. **37**, 3128–3132 (1998).
7. U. Wandinger and A. Ansmann, "Experimental determination of the lidar overlap profile with Raman lidar," Opt. Soc. Am. **41**, 511–514 (2002).
8. F. Navas, J. L. Guerrero-Rascado, and L. Alasdos-Arboledas, "Retrieval of the lidar overlap function using Raman signals," Opt. Pura Aplicada **44**, 71–75 (2011).
9. D. D. Venable, D. N. Whiteman, M. Calhoun, A. O. Dirisu, R. Connell, and E. Landulfo, "A lamp mapping technique for independent determination of the water vapor mixing ratio calibration factor for a raman lidar system," Appl. Opt. **50**, 4622–4632 (2011).
10. M. Walker, D. Venable, and D. N. Whiteman, "Gluing for Raman lidar systems using the lamp mapping technique," Appl. Opt. **53**, 8538–8543 (2014).
11. D. N. Whiteman, M. Cadirola, D. Venable, M. Calhoun, L. Miloshevich, K. Vermeesch, L. Twigg, A. Dirisu, D. Hurst, E. Hall, A. Jordan, and H. Vömel, "Correction technique for Raman water vapor lidar signal dependent bias and suitability for water vapor trend monitoring in the upper troposphere," Atmos. Meas. Tech. **4**, 7337–7403 (2011).
12. E. Hecht, "Modern optics: lasers and other topics," in *Optics*, 4th ed. (2001), pp. 581–648.
13. D. N. Whiteman, S. H. Melfi, and R. A. Ferrare, "Raman lidar system measurement of water vapor and aerosols in the Earth's atmosphere," App. Opt. **31**, 3068–3082 (1992).
14. J. R. Jenness, Jr., D. B. Lysak, Jr., and C. R. Philbrick, "Design of a lidar receiver with fiber-optic output," Appt. Opt. **36**, 4278–4284 (1997).
15. D. N. Whiteman, F. Russo, B. Demoz, L. M. Miloshevich, I. Veselovshii, S. Hannon, Z. Wang, H. Vomel, F. Schmidlin, B. Lesht, P. J. Moore, A. S. Beebe, A. Gambacorta, and C. Barnet, "Analysis of Raman lidar and radiosonde measurements from the AWEX-G field campaign and its relation to aqua validation," J. Geophys. Res. **111**, 1–15 (2006).
16. V. Simeonov, G. Larcheveque, P. Quagila, H. van den Bergh, and B. Calpini, "Influence of the photomultiplier tube spatial uniformity on lidar signals," Appl. Opt. **38**, 5186–5190 (1999).